# Photonic-Crystal Antenna Substrates

Elliott R. Brown, Oliver B. McMahon, and Christopher D. Parker

**A recently developed artificial dielectric, called a photonic crystal, provides an elegant and effective solution to the long-standing problem of fabricating high-performance planar antennas on substrates having high dielectric constants. The stop band of the photonic crystal rejects the majority of power radiated by an antenna mounted on its surface, without shorting out the driving-point impedance. This behavior makes the antenna more efficient than if it is mounted on a homogeneous substrate consisting of the same dielectric material as the photonic crystal. We experimentally measured antenna characteristics for bow-tie and dipole antennas on two types of photonic crystal: (1) conventional photonic crystals consisting of a periodic array of holes filled with air and embedded in a high dielectric material, and (2) metallodielectric photonic crystals (MDPCs) consisting of a periodic array of metallic spheres embedded in a low dielectric material. In some cases, experiments show that the directive gain can greatly exceed that of the same antenna suspended in free space.**

Radio-frequency engineers have long prized the planar antenna for its ability to couple incoming and outgoing radiation from microwave integrated circuits. Besides being more compact and less expensive than air-filled radiators (e.g., feed horns), a planar antenna allows for the integration of metallic radiators with transmit and receive electronics in the construction of phased arrays and synthetic apertures. A drawback, however, is that a planar antenna does not readily produce satisfactory gain or directivity when mounted on semiconductor substrates such as gallium arsenide or silicon. The high dielectric constant of these common semiconductors tends to trap radiation in the substrate, leading to degradation of the gain and directivity.

This article describes an approach for producing a more effective planar antenna on semiconductors or other substrates by transforming the substrate material into what is called a photonic crystal. This approach, which originated at Lincoln Laboratory in 1992, continues to be developed at the Laboratory and at other U.S. research institutions. The research has spawned additional applications of photonic-crystal substrates, such as band-rejection filters. In all cases, the photonic crystal imparts to the substrate a frequency and directional selectivity that is unique in the microwave field. This selectivity is a hallmark for a new branch of microwave engineering that we call functional substrates. In this branch, we work with a substrate that does much more than harbor radiation within transmission lines defined on its surface. The substrates can filter, tune, transform, match, and operate on radiation in ways traditionally left to reactive components and distributed circuits. Consequently, microwave and millimeter-wave integrated circuits can be made more compact and, we hope, can achieve superior performance in many applications.

## Fundamentals of Photonic Crystals

In general, photonic crystals are material structures whose electric or magnetic susceptibility varies periodically in one, two, or three dimensions. When such structures are illuminated by a beam having a wavelength comparable to the spatial period of the crystal, two effects occur. First, the variation of susceptibility within a period causes point-like electromagnetic scattering that can often be described by an angular-dependent cross section. Second, the periodic variation causes distributed scattering usually described by an electromagnetic dispersion relation (circular frequency $w$ versus wave vector $k$) that is modified substantially from the typical linear relation for propagation through linear, isotropic, and homogeneous materials. This modified form of scattering leads to the nomenclature of photonic crystal because the distributed scattering and modified dispersion relations that occur for photons are analogous to the distributed scattering and band dispersion that occur for electrons in an atomic crystal.

The understanding of distributed scattering of radiation goes back nearly a century to the seminal work of Bragg, Brillouin, and others. Their work led to numerous technological developments involving periodic structures in one dimension, including high- and low-reflectivity dielectric stacks for mirrors and windows. In fact, the high-reflectivity stack, sometimes called the distributed Bragg reflector, is now used in a variety of optoelectronic applications, including semiconductor diode lasers. Recent photonic-crystal research has been directed largely at extending features of one-dimensional distributed scattering, such as the electromagnetic stop band, to two and three dimensions.

The stop band is the basis of most photonic-crystal applications. It is characterized by a strong reflection of radiation over a certain frequency range, and high transmission outside this range. The center frequency, depth, and, to a lesser extent, width of a stop band are established by design. Hence we can tailor the stop band to specific circuit and component requirements.

The stop band represents a conceptual basis for comparing the properties of photonic crystals in different dimensions. By definition, the stop band is a range of frequency over which no propagation of radiation can occur, at least in the limit of an infinite crystal. Figure 1 shows that the stop band along the axis of periodicity of a one-dimensional photonic crystal will generally move in center frequency and degrade in reflection characteristic at angles away from this axis. In contrast, the stop band of a two-di-

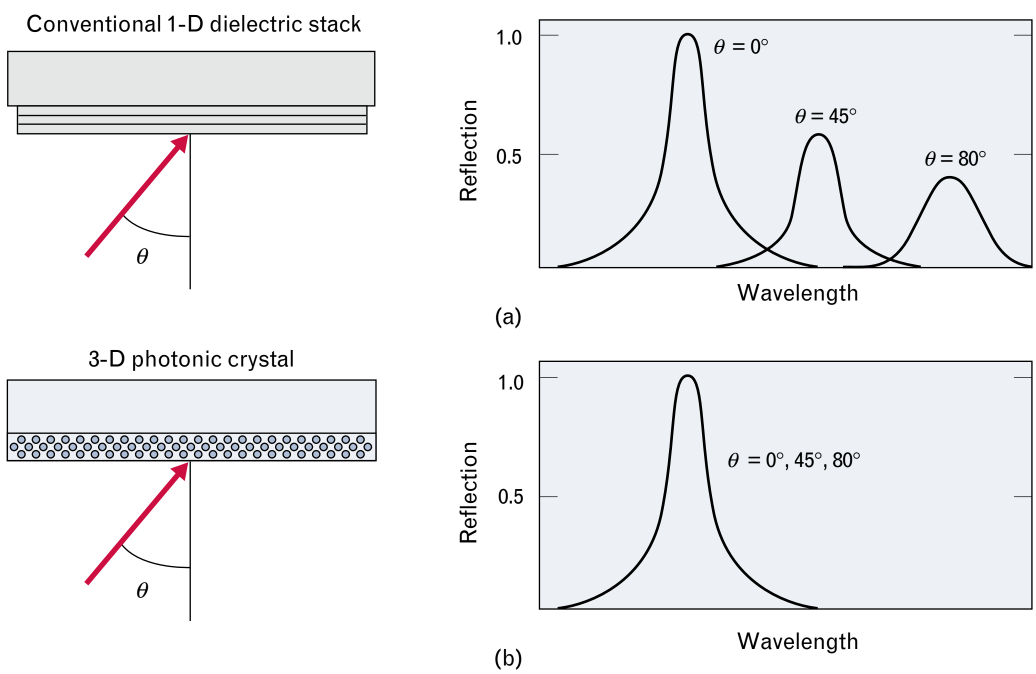


**FIGURE 1.** Comparison of stop-band behavior for radiation incident on one-dimensional (1-D) and three-dimensional (3-D) photonic crystals. (a) As the angle of incidence increases in a 1-D photonic crystal, the stop band moves in center frequency and degrades in reflection characteristic. (b) As the angle of incidence increases in a 3-D photonic crystal, the stop band maintains its frequency and reflection characteristic at all angles of incident propagation.

mensional photonic crystal can maintain its frequency and reflection characteristics with changing propagation angles lying in the plane of periodicity. The stop band of a three-dimensional photonic crystal can maintain its frequency and reflection characteristics at all angles of incident propagation.

In two- or three-dimensional photonic crystals, we refer to the stop band as a photonic band gap if it is maintained over the entire plane or sphere of periodicity. The photonic band gap has been the primary topic of debate on photonic crystals for more than ten years [1]. Initially, theorists questioned whether a photonic band gap could exist in dimensions higher than one. After suitable structures were found in three dimensions (diamond structure [2]) and two dimensions (hexagonal structure [3]), the quest has been to find other structures or material combinations leading to superior photonic band-gap characteristics and greater manufacturability.

In the context of photonic-crystal planar antennas, the existence of a photonic band gap is important because some antennas intrinsically emit or receive radiation over large solid angles, often a large fraction of a sphere. However, because highly directional antennas and most other practical microwave circuits and components operate over only a limited range of angles, other features of the photonic crystal become more important. For example, the width of the stop band and the absolute reflectivity inside and outside the stop band must be matched to other devices, passive and active, to meet overall circuit-performance requirements. In addition, the mechanical properties of the photonic crystal become important to achieve compatibility with the metallic antennas or transmission lines fabricated on its surface.

### *Three-Dimensional Photonic Band-Gap Structures*

The first photonic crystal to exhibit a three-dimensional stop band, or photonic band gap, was a (111)-axis-oriented face-centered-cubic (fcc) lattice with nonspherical air atoms. The crystal was fabricated at Bellcore from a cube of the synthetic dielectric material Stycast, which has a dielectric constant of 12 and a thickness of 8 cubic-lattice periods [4]. The photonic crystal was formed by drilling holes through each point on a triangular lattice on one facet of the cube.

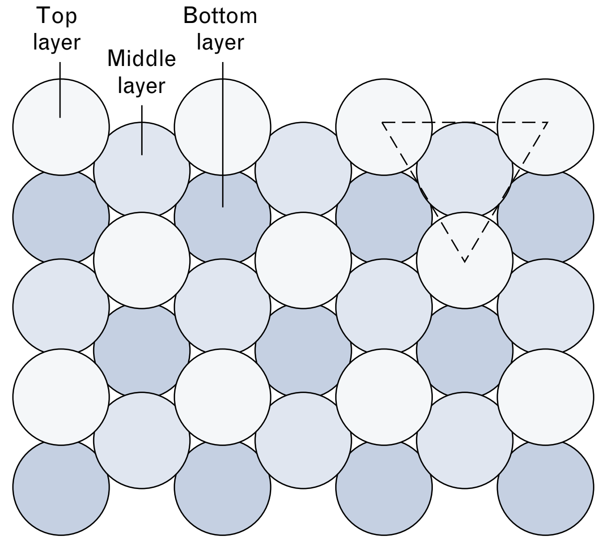


**FIGURE 2.** Topological view of the Lincoln Laboratory photonic crystal. Shaded circles represent the cylindrical atoms in three successive layers of the face-centered-cubic (fcc) lattice. Each atom in the middle layer lies directly below the center of a triangular unit cell consisting of atoms from the top layer. Each atom in the bottom layer lies directly below the centers of the remaining unit cells in the top layer.

The three holes were oriented at 54.7° from the normal direction and lay 120° apart in azimuth. About 80% of the Stycast was removed to produce a deep stop band extending from approximately 13.0 to 16.0 GHz. The depth of the stop band along the (111) axis was approximately 15 dB per cm of crystal thickness, corresponding to 12 dB per lattice constant.

More recently, it has been shown theoretically [5, 6] and experimentally [7] that a full photonic band gap can be obtained with a diamond-lattice structure. A microwave diamond photonic crystal was fabricated by stacking aluminum-oxide rods in a woodpile fashion. Transmission measurements through the stop band of this photonic crystal displayed a maximum stop-band attenuation of roughly 15 dB per lattice constant, substantially greater than the specific attenuation of the Bellcore Stycast fcc structure. The woodpile arrangement was also shown to be adaptable to downscaling achieved by using the technique of silicon bulk micromachining to create stop bands up to millimeter-wave frequencies [7].

At Lincoln Laboratory, we used a different technique to form an fcc photonic crystal from Stycast [8]. Figure 2 shows the vertical repeat unit of the fcc structure as three layers. Each atom in the middle layer lies directly below the center of a triangular unit cell consisting of atoms from the top layer. Each atom in the bottom layer lies directly below the centers of the remaining unit cells in the top layer. If the atoms were spherical and there were no intervening dielectric material, this stacking arrangement would result in the (111)-oriented fcc close-packed lattice [9]. This lattice constrains the triangular lattice constant $t$ to the slab thickness $s$ by the relation $t = (3/2)^{1/2}s$. The conventional cubic lattice constant $a$ is then $2^{1/2}t$. Because the atomic shape in this fcc structure is cylindrical, we do not expect the stop-band properties (or the band structure) to be the same at common symmetry points (i.e., the 6X points in the fcc Brillouin zone) [9]. Nevertheless, the structure displays a sizable stop band along the axis normal to the top facet (corresponding to one of the $L$-points [9] in the Brillouin zone) and over a large angle about the normal. Furthermore, the triangular lattice of the crystal is known to have good two-dimensional stop-band properties in the plane [3]. Hence this fcc structure is useful as a substrate for planar antennas or transmission lines operating at frequencies near the center of the first stop band.

### *Metallodielectric Photonic Crystals*

The stop band in the previously discussed photonic crystals generally has a width less than 25% of the center frequency and a maximum rejection less than 15 dB per lattice constant. The limited rejection follows partly from the fact that a significant fraction of radiation penetrates through the dielectric cores, so that backscattering from a given unit cell is expected to be weaker than forward scattering. As a result, distributed scattering is effective only when several unit cells exist along the direction of propagation.

To enhance rejection in the stop band, we can implement a more impenetrable core consisting of a metallic sphere. Because its dielectric constant has a large imaginary component, a metallic, spherical core can reflect radiation efficiently, at least at microwave and millimeter-wave frequencies, even when it is surrounded by high-permeability dielectric. For example, a (111)-oriented fcc lattice was constructed by stacking slabs of low-loss dielectric material of thickness $s$, each slab containing a triangular lattice of cylindrical air holes [8]. After the holes were fabricated in each slab, chrome-plated steel spheres were inserted, and the slabs were stacked in a close-packed fashion, as shown in Figure 3.

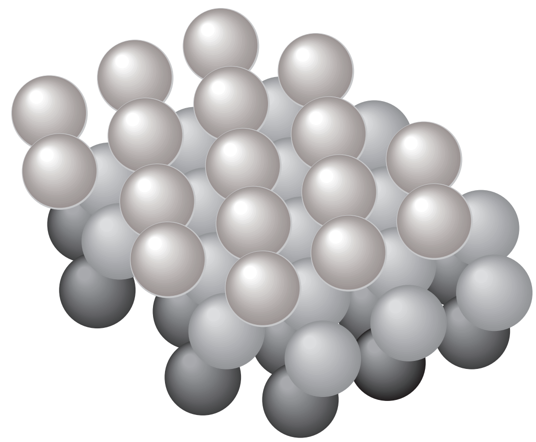

**FIGURE 3.** Perspective view of an fcc metallodielectric photonic crystal (MDPC) consisting of metallic spheres, in this case unsupported by a dielectric structure.

This structure is called a metallodielectric photonic crystal (MDPC) because the stop-band characteristics depend strongly on the size of the metal spheres as well as the dielectric constant of the supporting structure. An important consideration in the MDPC is that the metallic spheres in adjacent layers do not touch. If they did touch, electromagnetic scattering from the connected spheres would tend to differ from that of a single sphere, and the sample would tend to act like a three-dimensional metal-mesh structure [10]. In a sense, the MDPC is the Babinet complement [11] of the metal-mesh crystal with the added feature of having a support material that can be selected over a large range of dielectric constant. More important, however, is the fact that unconnected atomic cores do not allow long-range conduction currents. Such currents contribute ohmic losses that increase rapidly with frequency and make it difficult to create effective stop bands in the infrared or visible frequency bands.

## Electromagnetic Characterization of Photonic Crystals

Like any other passive microwave component, the photonic crystal can be characterized by scattering parameters $S_{ij}$, particularly the transmission coefficient $S_{21}$ and reflection coefficient $S_{11}$, and by insertion loss $L$, which are measured experimentally. These parameters are defined specifically for a propagating plane wave at incident angle $\theta$ and for the specular transmission and reflection angles, as shown in Figure 4. As such, these parameters are inherently a function of frequency and, for two- or three-dimensional crystals, of incident angle. At any given frequency and angle of incidence, the scattering coefficients satisfy $|S_{21}| + |S_{11}| + L = 1$, as in all passive components.

For a sufficiently thick photonic crystal at frequencies within the stop band, we expect the transmission coefficient to be well below unity and the reflection coefficient to be close to unity. At frequencies outside the stop band, we expect the reflection coefficient to be much lower, although not necessarily insignificant, and the transmission coefficient to depend strongly on the reflection and the bulk properties of the crystal. We cannot be sure what the insertion loss will be at any frequency because several factors influence it. An obvious factor is bulk attenuation due to absorption in the dielectric material of the photonic crystal. A less obvious factor is scattering of incident radiation into nonspecular angles on reflection or transmission. Such scattering can occur into free-space modes or into confined modes in the photonic crystals, such as evanescent modes at the air-crystal interfaces.

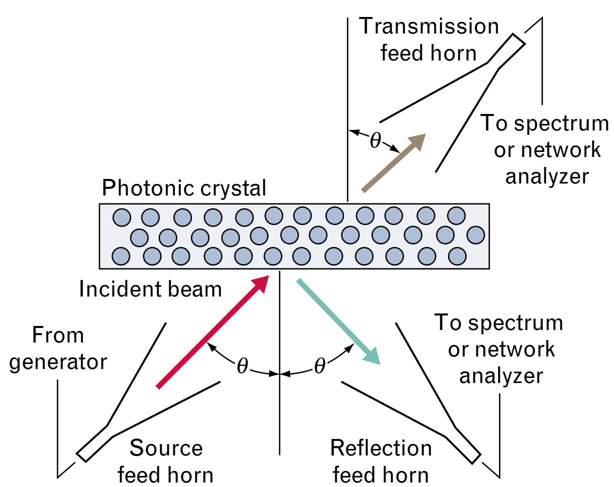


**FIGURE 4.** Experimental setup used to measure the transmission and reflection properties of photonic crystals. The crystals are characterized by their scattering parameters, which depend on beam frequency and scattering angle $\theta$.

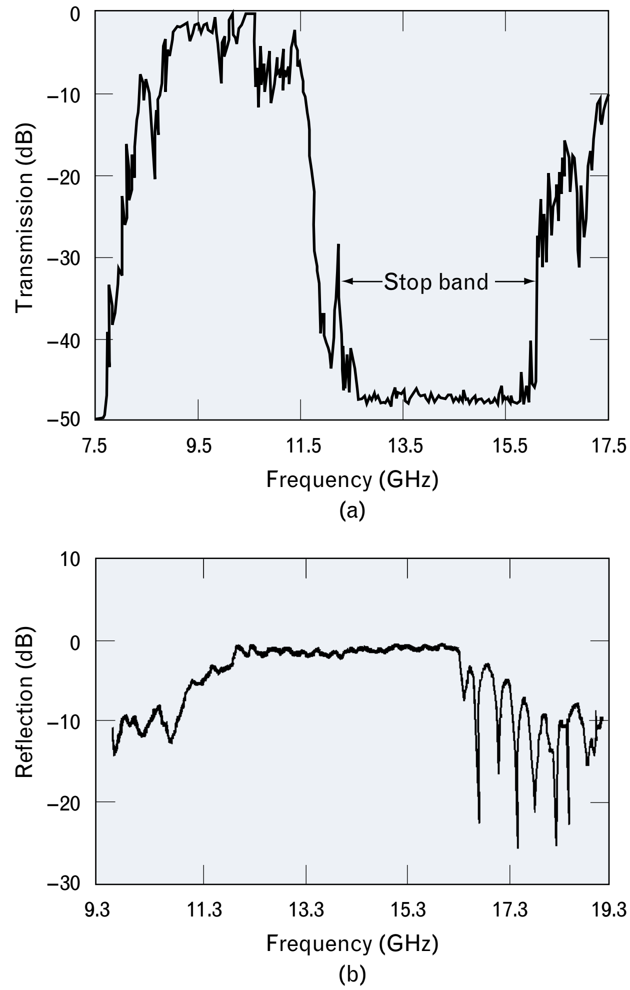


**FIGURE 5.** (a) Normal-incidence transmission spectrum and (b) reflection spectrum for the Bellcore Stycast fcc photonic crystal. The stop band is the range of low transmission from approximately 12 to 16 GHz.

The most important scattering characteristics of photonic crystals used as substrates for planar antennas are those along $\theta = 0$ because planar antennas typically radiate most strongly along the zenith. In this case the scattering parameters are adequately determined experimentally by using feed horns in the incident, reflected, and transmitted beams shown in Figure 4. The feed horns create a beam larger than a few unit cells but smaller than the lateral extent of the sample. This experiment approximates a plane-wave condition across a given unit cell of the crystal while avoiding spillover effects around the edges.

Figure 5 shows the transmission coefficient $T$ and the reflection coefficient $R$ from the Bellcore Stycast fcc photonic crystal at normal incidence. The stop band is recognized as the range of low transmission from approximately 12 to 16 GHz. Within the stop band, the transmission is between –45 and –50 dB, leaving the measurement just out of the instrument noise. In the lower pass band (down to approximately 8 GHz) the transmission varies between 0 and –10 dB, and in the upper pass band it is considerably lower.

Figure 5(b) shows that the reflection is consistent with the expected relation $R = 1 - T$. The reflection coefficient in the stop band is unity, within the resolution of the measurement. In the upper pass band, the reflection shows a sequence of broad peaks and sharp notches associated with longitudinal modes between the front and back facets of the sample [12]. The relatively strong reflection over these peaks causes the reduced transmission in this pass band.

Figure 6 shows the transmission spectrum through three lattice periods of the Lincoln Laboratory fcc photonic crystal for radiation at normal incidence. The sample was made from nine Stycast slabs having dimensions 0.64 × 15.2 × 15.2 cm (0.25 × 6.0 × 6.0 in). The cubic lattice constant of the sample was 1.10 cm. The stop band is readily recognized as the range of low transmission from roughly 17.4 to 18.2 GHz. Like most stop bands, it shows precipitous drops at the low-frequency and high-frequency ends. Within the stop band, two deep notches are centered between 17.5 and 18.0 GHz. The transmission associated with these notches is around –35 dB. Aside from this feature, the average transmission is about –25 dB, corresponding to a bulk rejection of 7.5 dB per cubic lattice constant.

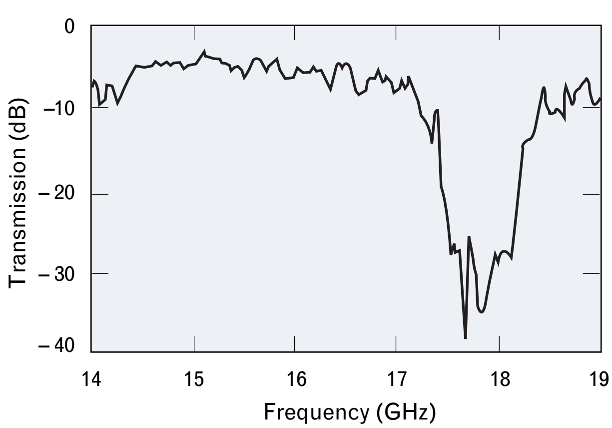


**FIGURE 6.** Normal-incidence transmission spectrum for the Lincoln Laboratory fcc photonic crystal relative to transmission in free space. The stop band is the range of low transmission from roughly 17.4 to 18.2 GHz.

The limited bulk rejection of this photonic crystal is a practical drawback. At less than 10 dB per cm, it takes too much material to meet the volumetric or weight limitations of many modern microwave components. This point is emphasized in Figure 7, which compares the normal-incidence transmission through a single period of the Stycast photonic crystal with transmission through free space and through an fcc MDPC sample. In this case, the first stop band of the Stycast crystal, centered around 17 GHz, is only about 10 dB deep. Note, however, the strong second stop band for the Stycast crystal centered around 23 GHz. Although this high-frequency stop band is attractive for components at higher microwave and millimeter-wave frequencies, most of the system applications tend to exist at Ku band and below, for which the MDPC is an inherently superior structure.

To demonstrate this superiority, we fabricated and measured an fcc MDPC by using the fcc Stycast crystal of Figure 7 as a basis. We transformed the fcc Stycast crystal into an fcc MDPC by inserting into each air-atom site a chrome-plated metal sphere. Figure 7 shows a deep, wide stop band from approximately 5.5 GHz to 12.5 GHz in the resulting transmission spectrum. Aside from undulations, the average rejection across this band is approximately 20 dB, which corresponds to 11.5 dB per cubic lattice constant. Above 13 GHz the MDPC returns to near-complete transmission, displays some localized dips, and then falls into another deep stop band starting at about 19 GHz.

Two aspects of this MDPC transmission are remarkable. First, the width $\Delta f = f_2 - f_1$ of the first stop band—approximately 74% about the center frequency $f_c = f_2 + f_1$—represents at least a fourfold increase over the stop-band width of any conventional photonic crystal. This increase is important for microwave applications, which often require at least one octave of instantaneous bandwidth ($\Delta f / f_c = 0.67$). Second, the transmission through the MDPC substrate in the first and second pass bands is near unity. This result surprised us because the MDPC consists

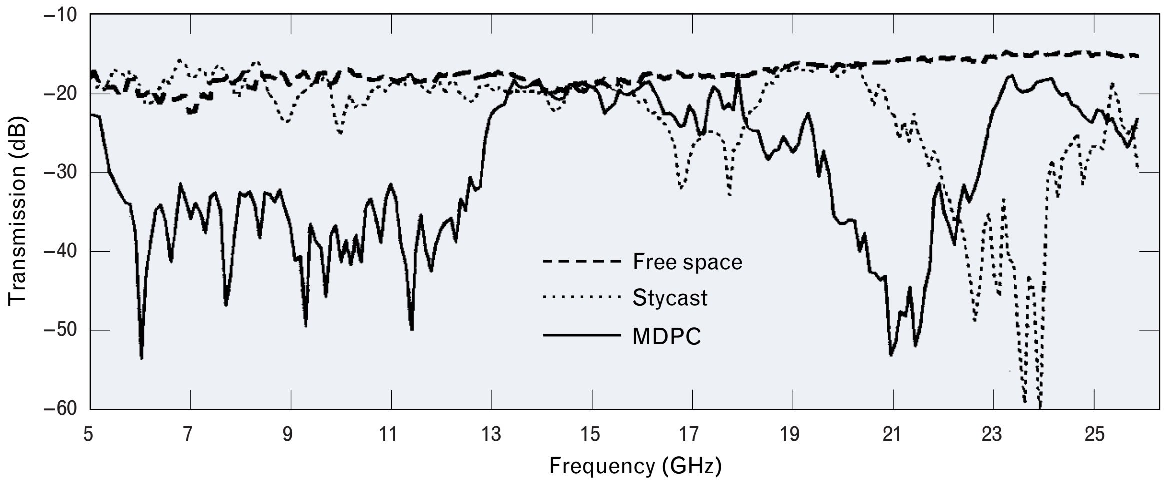


**FIGURE 7.** Comparison of normal-incidence transmission spectra for free space, the Lincoln Laboratory fcc Stycast crystal, and an fcc MDPC. The Stycast crystal exhibits two stop bands, the first centered around 17 GHz and the second centered around 23 GHz. The MDPC exhibits a deep, wide stop band from approximately 5.5 GHz to 12.5 GHz and a second stop band centered around 21 GHz.

mostly of metal that, in the form of a slab having the same lateral dimension, would reflect over 99% of the incident radiation in the given frequency range.

After observing the transmission through this MDPC, we hypothesized that the high dielectric constant of Stycast may be ineffective because the scattering within a unit cell of the material is probably dominated by the metal sphere. To test this hypothesis, we fabricated a Teflon MDPC with a dielectric constant $\varepsilon$ of 2.1 by using 1/4-in-thick slabs and 3/16-in-diameter spheres. Figure 8 shows the normal-incidence transmission spectrum, which appears to contain a broad stop band from approximately 14 GHz to above 20 GHz. This behavior corresponds to the broad stop band in the Stycast MDPC from approximately 5.5 to 12.5 GHz. It is not surprising that the center frequencies of the broad stop bands of the two samples—roughly 8.7 and 18.0 GHz, respectively—are in a proportion roughly equal to the ratio of the refractive index of Stycast to Teflon, 3.45 to 1.45, respectively. Ignoring the oscillations in the broad stop band of the Teflon MDPC, we find a maximum rejection within the stop band of roughly 12 dB (7 dB per cubic lattice constant). This rejection is comparable to that in conventional photonic crystals, but it spans a far greater bandwidth.

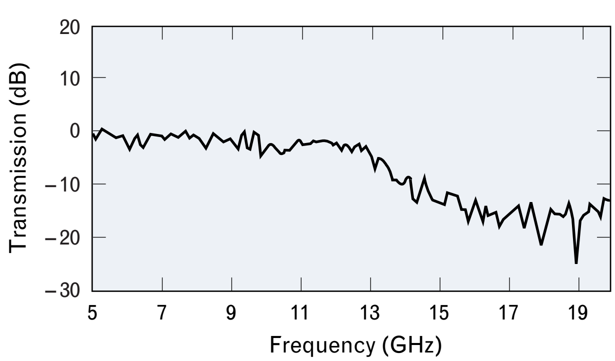


**FIGURE 8.** Normal-incidence transmission spectrum for a Teflon MDPC containing 3/16-in-diameter spheres. The spectrum shown is relative to the transmission of radiation in free space. A broad stop band ranges from approximately 14 GHz to above 20 GHz.

## Planar Antennas on Photonic-Crystal Substrates

When planar antennas are fabricated monolithically on a semiconductor substrate such as silicon, the resulting integrated circuit can be more compact and functional than alternative hybrid circuits. High-resistivity (approximately $10^4$ Ω-cm) silicon has weak enough absorptivity ($A < 0.2$ cm$^{-1}$) to be useful up to millimeter-wave frequencies (>30 GHz) [13]. However, a silicon substrate has a high dielectric constant $\varepsilon$ of 11.8, which makes the performance of a planar antenna on its surface inferior to that of a similar antenna in free space. The performance decrease is one reason that air-filled antennas, such as feed horns and helices, continue to be used in the majority of microwave and millimeter-wave applications requiring high directive gain.

The problems associated with planar antennas on semiconductor substrates originate in the fundamental electromagnetics of a conductor on a dielectric surface. Figure 9(a) shows the conductor-substrate interface for a generic metallic planar antenna on a homogeneous substrate having a purely real dielectric function (i.e., no electromagnetic attenuation) represented by the dielectric constant $\varepsilon$. The antenna has a tendency independent of its shape to radiate more power into the substrate than into the free space above the substrate. The ratio of the power into the substrate to the power into free space increases as the dielectric constant $\varepsilon$ increases. For example, an infinitesimal planar dipole radiates approximately $\varepsilon^{3/2}$ more power into the substrate than into free space [14]. Thus a dipole on a silicon substrate with $\varepsilon$ of 11.7 radiates approximately forty times more power into the substrate. A second problem is that the power radiated into the substrate at angles greater than the critical angle $\theta_c = \sin^{-1}\varepsilon^{-1/2}$ is totally internally reflected at the top and bottom substrate-air interfaces. For silicon, total internal reflection occurs at $\theta_c \approx 17°$, meaning that most of the radiated power in many antenna structures is trapped in the substrate, as shown in Figure 9(a).

In contrast, Figure 9(b) shows the behavior of a planar antenna on a photonic-crystal substrate. If the driving frequency of the antenna lies within the photonic band gap, we expect that no power will be radiated into the substrate at any angle, since at every point along the conductor-substrate interface no propagation is allowed over the full hemisphere on the substrate side. However, it is not clear what fraction of the driving power will be radiated into the air side, because evanescent modes still exist at the air-substrate interface [15], and impedance mismatch can reflect power back to the generator.

### *Fabrication and Measurement Techniques*

We fabricated two types of planar antennas in early studies: bow ties (i.e., long, tapered dipoles) and resonant dipoles. These antennas were fabricated with either thin copper tape attached directly to the surface or freestanding metal shimstock abutted to the crystal. An amplitude-modulated generator with a coaxial output port drove the antennas. Feed lines were routed to the planar antenna with a line-stretcher-type phase shifter added in one line to achieve a balanced drive at the end. We determined the degree of balance by adjusting the line stretcher to minimize the power in the unused port of the hybrid.

The radiation patterns from these antennas were measured with a compact antenna test range. The photonic crystal was mounted on one end of the range in a plastic mounting yoke designed to rotate in elevation and azimuth by onboard metal gear assemblies. Microwave absorbing foam shielded the gears from the photonic crystal. We measured the electric *E*-plane pattern of a dipole by rotating the mounting yoke through 180° in elevation. The mounting yoke was then rotated 180° in azimuth to obtain the mag-

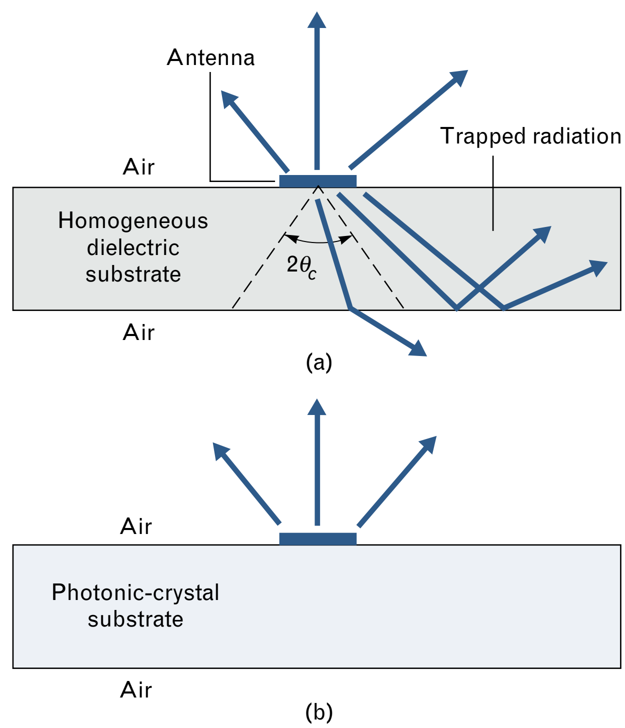


**FIGURE 9.** Generic behavior of a planar antenna on substrates. (a) For the homogenous substrate, the antenna tends to radiate more power into the substrate than into the free space above the substrate. Total internal reflection occurs at angles greater than the critical angle $\theta_c$. (b) For the photonic-crystal substrate, if the driving frequency of the antenna is in the photonic band gap, no power will be radiated into the substrate at any angle because at every point along the conductor-substrate interface propagation does not occur over the full hemisphere on the substrate side.

netic *H*-plane pattern. The radiated power was collected by a scalar receiver consisting of a pyramidal feed horn connected to a rectangular waveguide; a waveguide-to-coaxial transition; a distributed amplifier; and a microwave detector diode. The separation between the planar antenna and the mouth of the receiver feed horn was approximately 1.4 m. The output of the diode was synchronously detected with a lock-in amplifier tuned to the AM frequency of the generator to enhance the measurement sensitivity.

### *First Planar Antenna on a Photonic-Crystal Substrate*

We fabricated the bow-tie antenna as our first planar antenna on a photonic crystal because of the antenna's inherently wideband behavior and nonreactive impedance properties on homogeneous dielectric substrates. A bow-tie antenna with a 45° flare angle was mounted first on a homogeneous block of Stycast that acted as the control sample, and then on the Bellcore fcc photonic crystal. In this early experiment, we paid little attention to how the driving point of the bow-tie antenna was placed in a unit cell or how the bow-tie antenna was oriented relative to the crystallographic axes.

Figures 10 and 11 show the radiation patterns for the homogeneous Stycast substrate and the photonic-crystal substrate, respectively, in polar plots having identical (linear) radial scales. The *E*-plane pattern of the homogeneous-substrate antenna, shown in Figure 10(a), is roughly twenty times more intense along the nadir than along the zenith. Similar behavior was observed in the *H*-plane pattern of Figure 10(b). The vast majority of the radiation was directed into the substrate, as in the discussion of the previous section.

The same bow-tie antenna displayed radically different *E*- and *H*-plane patterns when mounted on the Bellcore fcc photonic crystal. Figure 11(a) shows the *E*-plane pattern dominated by two sidelobes, similar to bow ties in free space, each sidelobe peaking approximately 35° down from the zenith. Figure 11(b) shows the *H*-plane pattern dominated by a zenithal lobe, also similar to a free-space bow tie. Although the patterns are scalloped, the vast majority of the radiated power is directed into the upper side of the crystal. Only a small spur of radiation is seen in the photonic-crystal side, represented by the lone data point in the *E*-plane pattern of Figure 11(a). Correspondingly, the radiation along the zenith is approximately thirty times more intense than the zenithal radiation on the homogeneous crystal characterized in Figure 10. This experiment represents the first demonstration of a photonic crystal suppressing radiation into the substrate and redirecting it into free space.

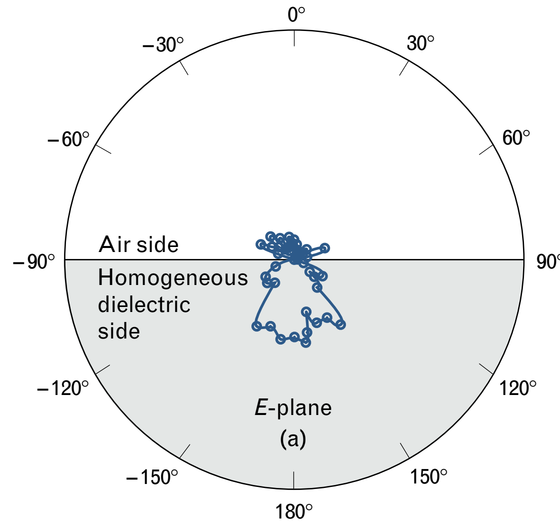


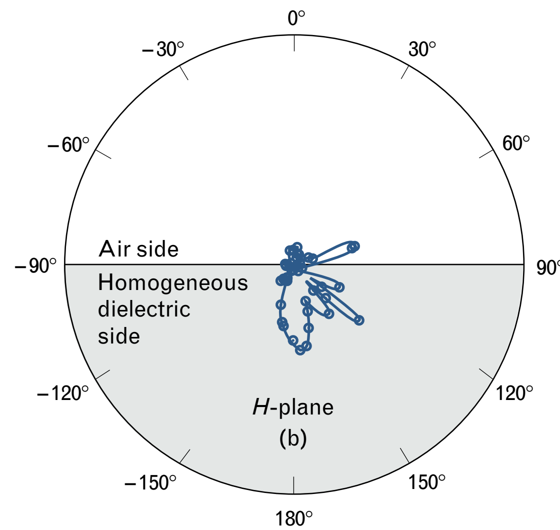


**FIGURE 10.** Far-field radiation patterns of a bow-tie antenna on a homogeneous Stycast substrate having a dielectric constant $\varepsilon$ of 12 for a driving frequency of 13.2 GHz. Normalized power is displayed on a linear scale. (a) *E*-plane pattern and (b) *H*-plane pattern. The *E*-plane pattern of the homogeneous-substrate antenna is roughly twenty times more intense along the nadir than along the zenith. The *H*-plane pattern shows the same behavior. Overall, the vast majority of radiation is directed into the substrate.

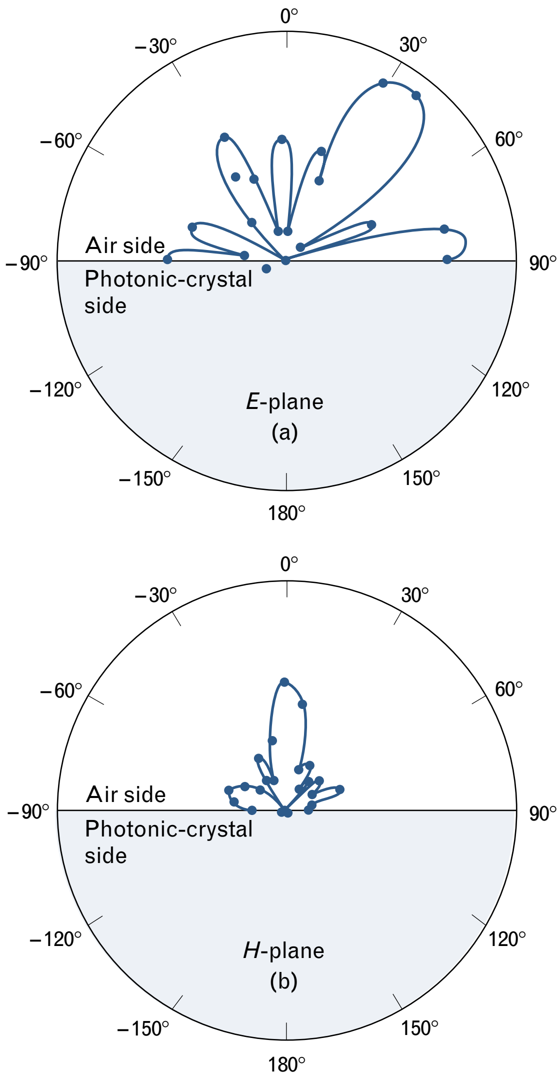


**FIGURE 11.** (a) *E*-plane and (b) *H*-plane far-field radiation patterns of a bow-tie antenna on a Bellcore fcc photonic crystal having a dielectric constant of 12 for a driving frequency of 13.2 GHz. Normalized power is displayed on a linear scale. The vast majority of radiated power is directed into the upper side of the crystal. A small spur of radiation is represented by the lone data point in the photonic-crystal side of the *E*-plane pattern. The radiation along the zenith is approximately thirty times more intense than the zenithal radiation on the homogeneous crystal of Figure 10.

Further qualitative analysis of Figures 10 and 11 suggests that more total power was being radiated into free space from the photonic-crystal substrate than from the homogeneous substrate. We attribute this difference in part to a better impedance match (and hence higher gain) between the generator and antenna on the photonic crystal. We also attribute the difference to the fact that a significant fraction of the radiation directed into the homogeneous Stycast substrate underwent multiple total internal reflections. Such radiation could then have been absorbed over the long path length or it could have been directed into the lower-side hemisphere along angles not lying in either the *E*- or *H*-planes and hence would not have been measured.

### *Planar Dipole on Photonic Crystal Substrates*

Although attractive in terms of bandwidth and impedance match, the bow-tie antenna proved too fragile to calibrate in free space and could not be easily moved around on the substrate to investigate the effect of driving-point position or antenna crystallographic orientation. A better antenna for these purposes, and one having a simpler intrinsic radiation pattern, was the strip dipole. Figure 12 shows that the overall length of the dipole equals one-half of a free-space wavelength at the drive frequency of 17.4 GHz. The dipole's intrinsic patterns in the *E*- and *H*-planes, shown in red in Figure 13, were measured while the dipole was suspended in free space. The *E*-plane pattern exhibits a peak intensity along the zenith ($\theta$ = 90°, $\phi$ = 90°) and falls rapidly with $\theta$ away from that direction. In the *H*-plane the radiation intensity is roughly constant out to an angle approximately 70° down from the zenith, where the radiation intensity exhibited a local peak followed by a rapid drop at higher angles. Ignoring this effect in the *H*-plane, which was most likely caused by interference with the coaxial feed lines, we fitted the *E*- and *H*-plane patterns with the following well-known expressions for a resonant half-wave dipole [16]:

$$\text{For } E\text{-plane} \quad S(\theta, \phi = 90°) = S_0 \frac{\cos^2[(\pi/2)\cos\theta]}{\sin^2\theta} ;$$

$$\text{For } H\text{-plane} \quad S(\theta = 90°, \phi) = S_0 ,$$

where $S$ is the radiation intensity (power per unit solid angle) and $S_0$ is the peak value. Comparing these expressions with the experimental curves at $q$ = 90° leads to a value of $S_0$ = 1.89. The same expressions yield a directivity of the free-space dipole in the *E*- plane:

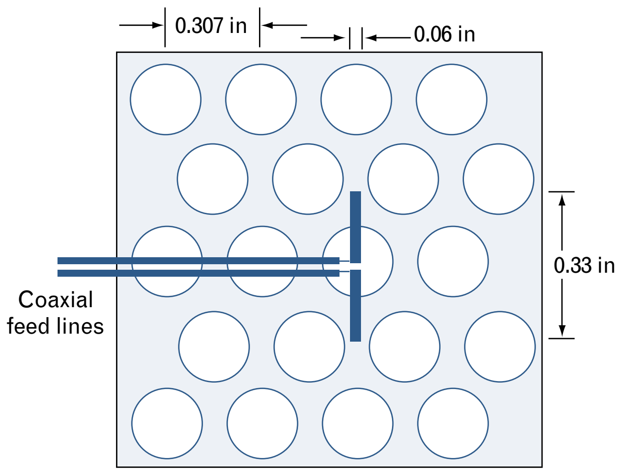


**FIGURE 12.** Schematic diagram of a strip dipole on the top facet of the Lincoln Laboratory fcc photonic crystal.

$$D(\theta, \phi = 90°) \equiv \frac{S(\theta, \phi = 90°)}{\int \frac{S(\theta, \phi) d\Omega}{4\pi}} = \frac{\cos^2[(\pi/2)\cos\theta] / \sin^2\theta}{0.609},$$

which has a maximum of 1.64 at the zenith.

The dipole was then mounted on the surface of the photonic crystal, and several different orientations relative to the unit cell of the fcc lattice were investigated. The best pattern with respect to intensity around the zenith was obtained for the dipole mounted with its driving point located directly over a cylindrical air atom, and oriented along a line through next-nearest neighbors of the surface triangular lattice, as shown in Figure 12. The resulting *E*-plane pattern in blue in Figure 13(a) is substantially different in angular dependence and magnitude from the free-space pattern displayed in the same figure. The photonic-crystal dipole exhibits a strong central lobe as well as secondary lobes at approximately 30° down from the zenith and weaker tertiary lobes centered about 70° from the zenith on either side. Outside of the tertiary lobes, the power drops more than 10 dB below the main lobe.

With respect to radiation magnitude, the dipole on the photonic crystal exhibited an intensity 5.5 times greater than that of the free-space dipole at the zenith. Because the drive conditions did not change in the

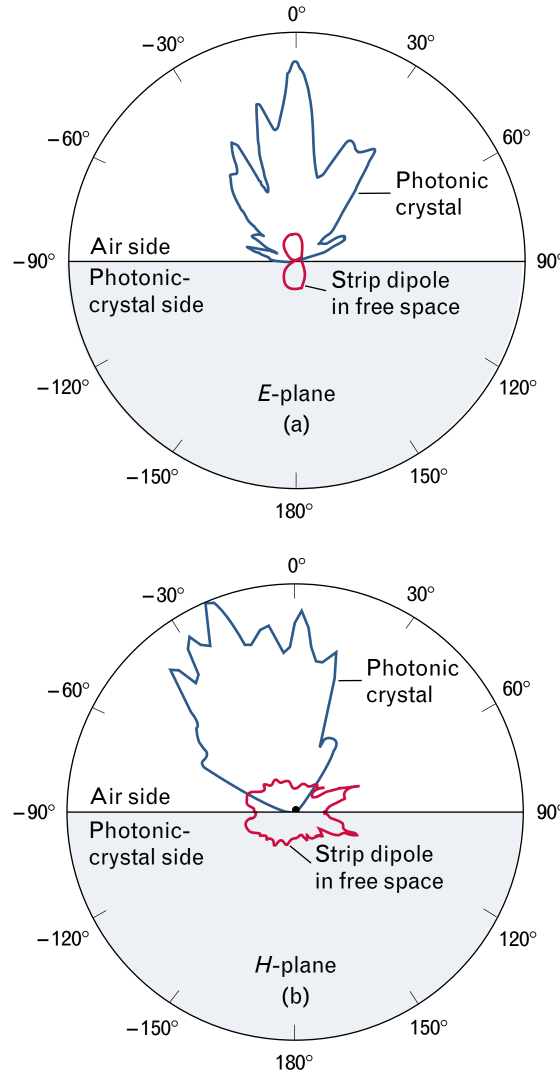


**FIGURE 13.** (a) *E*-plane radiation pattern from a strip dipole on the Lincoln Laboratory fcc photonic crystal and the same dipole in free space for a driving frequency of 17.4 GHz. The photonic-crystal dipole exhibits a strong central lobe as well as secondary lobes at approximately 30° down from the zenith and weaker tertiary lobes centered about 70° from the zenith on either side. (b) *H*-plane radiation pattern. Although roughly constant from the zenith out to approximately 20° on either side, the intensity of strip-dipole radiation drops rapidly at larger angles at a rate comparable to the intensity decay in the *E*-plane.

process, this intensity corresponded to a directivity *D* of 9.0. Figure 13(b) shows the *H*-plane pattern of the photonic-crystal dipole, which also differed substantially from its free-space counterpart. Although roughly constant from the zenith out to approximately 20° on either side, the intensity dropped rapidly at larger angles at a rate comparable to the intensity decay in the *E*-plane. The *H*-plane pattern also exhibited the highest directivity observed for this combination of dipole and photonic crystal: $D = 10.1$ approximately 20° down from the zenith. We suspect that feed-line interference caused the maximum directivity to occur away from the zenith.

To convert the directivity of the free-space and photonic-crystal dipoles into radiative gain, we used the relation

$$G(\theta, \phi) = (1 - \rho)(1 - A)D(\theta, \phi) ,$$

where $\rho$ is the power reflectivity and $A$ is the absorptivity (the fraction of incident power that is either absorbed by the antenna element or feed lines, radiated into a cross-polarized pattern, or radiated into surface modes when the photonic crystal is present). We measured the reflectivity of the antennas with a network analyzer, and deduced the absorptivity from the total radiated power. The reflectivity $\rho$ was found to be 0.16 (–8.0 dB) and 0.13 (–9 dB) for the free-space and photonic-crystal dipoles, respectively. Hence the photonic crystal created a 1-dB improved impedance match to the 50-Ω generator.

We estimated the absorptivity $A$ by comparing the total radiated power to the incident generator power, taking into account the finite reflectivity. For the free-space dipole, we deduced the total radiated power from the analytic expressions stated earlier in this section and by using the measured zenithal intensity $S_0$ to set the scale. This comparison led to $A = 0.09$ and $G(\theta = 90°) = 1.25$. The absorptivity of the photonic-crystal dipole was more difficult to determine because we did not know the radiation intensity away from the *E*- and *H*-planes. Consequently, we integrated over the hemisphere by using the *E*-plane intensity pattern in $\theta$ for each cut in $\phi$ with a weighting factor equal to the *H*-plane intensity at that $\phi$ divided by the zenithal intensity. This technique gave us the result $A = 0.08$, with an uncertainty of approximately 20% from the pattern integration. By using this absorptivity along with $R = 0.13$ and the values of directivity noted above, we calculated a zenithal gain of 7.2, which is 5.8 times that of the free-space dipole.

Similarly, we found a peak gain of 8.1 in the *H*-plane 20° from the zenith. We determined by rough measurements that the major contribution to the normal absorptivity was cross-polarized radiation. Such cross-polarization was also found with the free-space dipole. For both the photonic-crystal and free-space cases, we attributed this effect to a slight deviation from colinearity of the two dipole arms.

Realizing that a conventional photonic crystal could enhance the zenithal intensity of a planar dipole in free space by as much as 5.8 times, we conceived of separate experiments to validate this enhancement. First, a free-space dipole was combined with a metallic ground plane, which was placed parallel to the dipole strips and placed approximately one-quarter wavelength behind the dipole. The separation was fine tuned to maximize the zenithal intensity measured in the antenna test range. The experimental

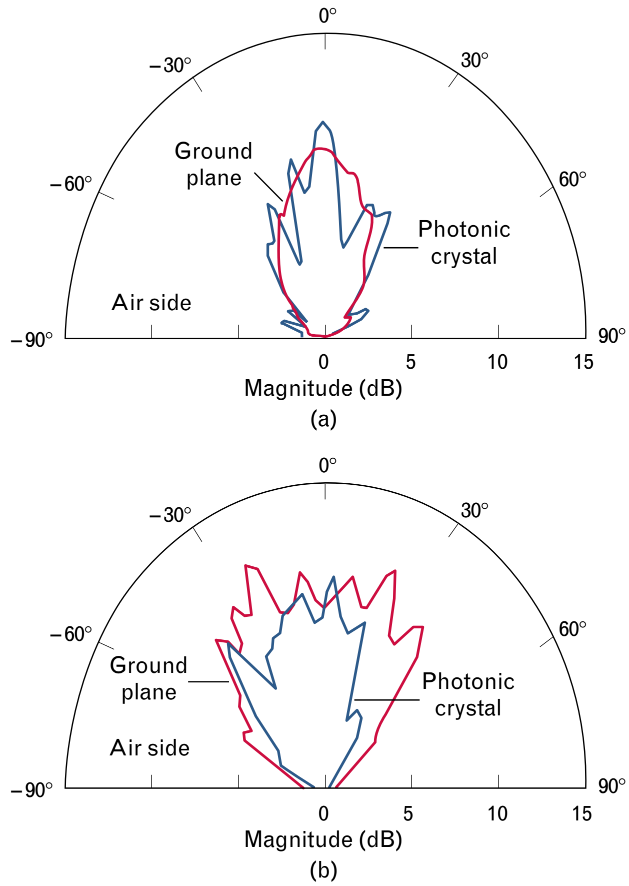


**FIGURE 14.** (a) *E*-plane radiation pattern from a strip dipole on the Lincoln Laboratory fcc photonic crystal and the same dipole in free space but one-quarter wavelength above a ground plane. (b) *H*-plane radiation pattern for the same configuration.

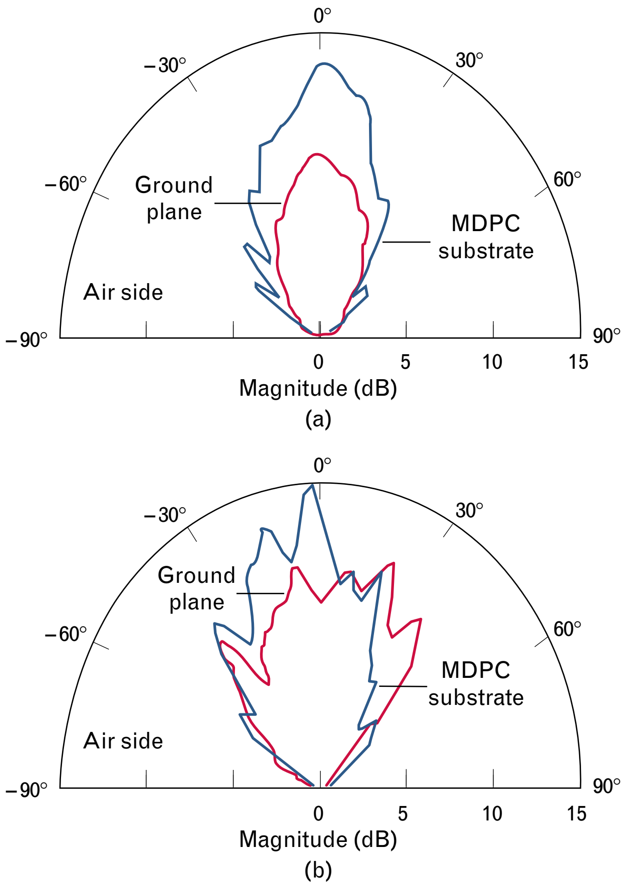


**FIGURE 15.** (a) *E*-plane radiation pattern from a strip dipole on an MDPC substrate and the same dipole in free space but one-quarter wavelength above a ground plane. (b) *H*-plane radiation pattern for the same configuration.

radiation patterns in the *E*- and *H*-planes are shown in Figure 14. In both planes, the zenithal intensity is approximately 5.1 times that of the dipole in free space, which is shown in Figure 13. A fourfold increase would be expected from the effect of constructive interference off the ground plane. We attributed the remaining increase to an improvement in impedance match between the generator and the antenna in the presence of the ground plane.

Superimposed in Figure 14 are the dipole patterns with the conventional photonic crystal. In both planes, we see that the crystal yields greater zenithal intensity than the optimized ground plane by approximately 10%. This trend was the first indication that something extraordinary might be occurring in the substrate reflection process. Our hypothesis was that the photonic crystal focuses the radiation somewhat like a curved mirror through the constructive scattering from multiple, nonparallel Bragg planes. The secondary and tertiary lobes in Figure 14(a) are consistent with this hypothesis.

Next, we investigated the same strip dipole depicted in Figure 12 with the Teflon MDPC described in the section "Metallodielectric Photonic Crystals." We wanted to determine the impact of the superior reflectivity of the MDPC per unit length; Figure 15 shows the *E*- and *H*-plane patterns of this antenna. Remarkably, the zenithal intensity was approximately 40% higher than that of the optimized free-space dipole above the ground plane, meaning that the zenithal gain was approximately 8.8, or 9.4 dB.

Another interesting feature of the strip dipole on an MDPC substrate was the reduction in sidelobe intensity, particularly in the *E*-plane patterns of Figure 15(a), compared to the patterns on the conventional photonic crystal shown in Figure 14. Although theoretical work is still under way to explain this reduction, it is plausible that the sidelobes are small because Bragg scattering plays a much weaker role in the MDPC substrate. Instead, most of the scattering amplitude, and hence the attenuation per unit length, arises from scattering within a unit cell. As we discuss next, at least part of the unit cell scattering is Mie scattering from the atomic core (i.e., metal spheres).

We intuitively expect that the superior gain of the MDPC substrate must be related to the fundamental differences in electromagnetic scattering between dielectric and metallic materials. In the simple case of spherical geometry, research earlier in this century demonstrated that dielectric and metallic spheres both exhibit little effect on electromagnetic radiation at wavelengths much greater than the diameter of the sphere. As the wavelength decreases, both types of spheres begin to scatter much more efficiently. In fact, the scattering cross section $\sigma$ varies with wavelength $\lambda$ as $1/\lambda^4$, according to Rayleigh's well-known relation. What distinguishes dielectric from metallic spheres is the strength and direction of the scattering. For a dielectric sphere, the total amount of scattering at a given wavelength is always much weaker than for a metal sphere of the same diameter. Furthermore, Mie's work showed that at wavelengths slightly greater than the sphere diameter, most of the radiation scattered from dielectric spheres goes into the forward hemisphere [17]. In contrast, at the same wavelength condition on metallic spheres most of the scattering occurs into the reverse hemisphere, even though there is a small Mie effect.

Another relevant result of Mie's work was that the scattering cross section $\sigma$ approaches a maximum when the wavelength satisfies the condition $\pi d/\lambda = 1$, where $\lambda = \lambda_0/n$ is the wavelength in the dielectric medium (for refractive index $n$) immediately surrounding the sphere of diameter $d$, and $\lambda_0$ is the wavelength in free space. For example, we consider the Teflon MDPC substrate used for the above antenna experiments in which $d = 3/16$ in, and $n = (2.1)^{1/2}$. In this case, we find a Mie frequency of $c/\pi dn = 13.8$ GHz, where $c$ is the speed of light. This prediction agrees with the low-frequency edge of the experimental stop band discussed earlier.

## Summary

The existence of a three-dimensional stop band in photonic crystals enables the unique application of a photonic crystal as a planar-antenna substrate because antennas naturally behave like three-dimensional radiators. In addition, the fact that the reflection is distributed means that the antenna does not short out at the driving point, as do planar antennas mounted directly on metal. Two types of photonic crystals have been shown to work in this way: (1) conventional (all-dielectric) crystals and (2) metallodielectric photonic crystals.

We demonstrated that a strip dipole on both types of crystals radiated far more intensely at the zenith than in free space, with only 10% of the radiation attributable to a better impedance match to the generator. Clearly, this enhancement is attributable to constructive specular reflection from the photonic crystal in the same fashion that a roughly fourfold enhancement occurs for a filamentary dipole placed at a quarter-wavelength distance above a ground plane. However, our work has shown that different photonic crystals carry out this reflection in different ways. The conventional photonic crystals appear to rely more on distributed scattering from Bragg planes. In contrast, the metallodielectric structures rely more on local scattering within a unit cell of the crystal. Detailed understanding of these reflection processes must wait for thorough theoretical and analytical efforts. We can already say that the performance in terms of zenithal substrate gain is good enough to warrant consideration in microwave and millimeter-wave applications, particularly those which require or profit from the implementation of planar antennas on substrates with high dielectric constants such as gallium arsenide or silicon.

## Acknowledgments

We acknowledge programmatic support for this work from the U.S. Army Research Office.

# REFERENCES

1. E. Yablonovitch, "Inhibited Spontaneous Emission in Solid-State Physics and Electronics," *Phys. Rev. Lett.* **58** (20), 1987, pp. 2059–2062.
2. K.M. Ho, C.T. Chan, and C.M. Soukoulis, "Existence of a Photonic Gap in Periodic Dielectric Structures," *Phys. Rev. Lett.* **65** (25), 1990, pp. 3152–3155.
3. R.D. Meade, K.D. Brommer, A.M. Rappe, and J.D. Joannopoulos, "Existence of a Photonic Band Gap in Two Dimensions," *Appl. Phys. Lett.* **61** (4), 1992, pp. 495–497.
4. E. Yablonovitch, T.J. Gmitter, and K.M. Leung, "Photonic Band Structure: The Face-Centered-Cubic Case Employing Nonspherical Atoms," *Phys. Rev. Lett.* **67** (17), 1991, pp. 2295–2298.
5. K.M. Ho, C.T. Chan, C.M. Soukoulis, R. Biswas, and M. Sigalas, "Photonic Band Gaps in Three Dimensions: New Layer-by-Layer Periodic Structures," *Solid State Commun.* **89** (5), 1994, pp. 413–416.
6. H.S. Sözüer and J.P. Dowling, "Photonic Band Calculations for Woodpile Structures," *J. Mod. Opt.* **41** (2), 1994, pp. 231–239.
7. E. Özbay, E. Michel, G. Tuttle, R. Biswas, M. Sigalas, and K.-M. Ho, "Micromachined Millimeter-Wave Photonic Band-Gap Crystals," *Appl. Phys. Lett.* **64** (16), 1994, pp. 2059–2061.
8. E.R. Brown, K. Agi, C.D. Dill III, C.D. Parker, and K.J. Malloy, "A New Face-Centered-Cubic Photonic Crystal for Microwave and Millimeter-Wave Applications," *Microw. Opt. Tech. Lett.* **7** (17), 1994, pp. 777–779.
9. N.W. Ashcroft and N.D. Mermin, *Solid State Physics* (Holt, Rinehart and Winston, New York, 1976).
10. D.F. Sievenpiper, M.E. Sickmiller, and E. Yablonovitch, "3D Wire Mesh Photonic Crystals," *Phys. Rev. Lett.* **76** (14), 1996, pp. 2480–2483.
11. N. Born and E. Wolf, *Principles of Optics: Electromagnetic Theory of Propagation, Interference, and Diffraction of Light,* 5th ed. (Pergamon, New York, 1975), sec. 11.3.
12. J.-P. Mattia, private communication.
13. M.N. Afsar and K.J. Button, "Millimeter-Wave Dielectric Measurement of Materials," *Proc. IEEE* **73** (1), 1985, pp. 131–153.
14. D.B. Rutledge, D.P. Neikirk, and D.P. Kasilingam, "Integrated-Circuit Antennas," in *Infrared and Millimeter Waves, Vol. 10: Millimeter Components and Techniques, Pt. II,* K.J. Button, ed. (Academic, New York, 1983), pp. 1–90.
15. R.D. Meade, K.D. Brommer, A.M. Rappe, and J.D. Joannopoulos, "Electromagnetic Bloch Waves at the Surface of a Photonic Crystal," *Phys. Rev. B* **44** (19), 1991, pp. 10 961–10 964.
16. R.S. Elliott, *Antenna Theory and Design* (Prentice-Hall, Englewood Cliffs, N.J., 1981).
17. Born and Wolf, *Principles of Optics*, sec. 13.5.

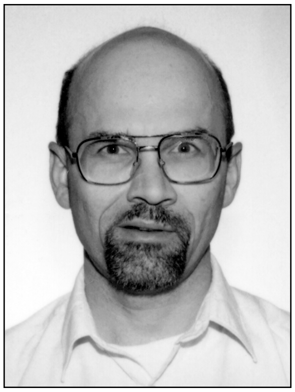

**ELLIOTT R. BROWN**
is professor of electrical engineering at the University of California, Los Angeles (UCLA), and a part-time technical staff member at the Jet Propulsion Laboratory in Pasadena, California. He develops research projects in power electromagnetics, ultrafast electronics and optoelectronics, advanced RF sensor technology, and biomedical engineering. Before joining UCLA, Elliott worked at the Defense Advanced Research Projects Agency (DARPA) in Arlington, Virginia, on programs in RF technology, high-power solid state electronics, highly controlled infrared dielectric emissivity, and acoustics. Before joining DARPA, Elliott was an assistant leader of the High-Speed Electronics group at Lincoln Laboratory, researching and developing ultrafast electronics and optoelectronics, advanced electromagnetics, solid state device physics, and high-frequency receiver technology. His discoveries include the resonant-tunneling-diode relaxation oscillator, the photonic-crystal planar antenna, the low-temperature-grown-GaAs THz photomixer, normal-incidence absorption in semiconductor quantum wells, and shot-noise suppression and quantum-transport inductance in resonant-tunneling devices. He holds a B.S. degree in physics from UCLA, and M.S. and Ph.D. degrees in applied physics from the California Institute of Technology.

**OLIVER B. MCMAHON**
is a principal test-design engineer at Sanders, a Lockheed Martin Company, where he is responsible for designing automated testing systems for electronic countermeasure systems for military aircraft. Prior to joining Sanders in 1997, he worked in the High-Speed Electronics group at Lincoln Laboratory on the development of a millimeter-wave radiometer for the remote detection of oil spill thickness; design, construction and testing of frequency-selective materials (photonic crystals); design of computer-controlled experiments and data acquisition; and CAD work for photomixer devices. As a programmer analyst for the Systems Analysis group at the Laboratory, Oliver wrote radar-simulation software. Before joining Lincoln Laboratory in 1988, Oliver worked for Merv Larson Co., Bronx, New York, as an exhibit construction artist for the Jungle World building in the Wild Asia section of the Bronx Zoo. At Adventureland Amusement Park in Farmingdale, New York, he sculpted patterns for architectural ornaments, performed fiberglass casting of finished pieces, and restored the carousel and other rides. Oliver holds a B.S.E.E. degree in electrical engineering from Manhattan College, Riverdale, New York, and a B.F.A. degree with an art education minor from Southampton College.

**CHRISTOPHER D. PARKER**
is a consultant to the Electro-Optical Materials and Devices group, studying the stability of the new quantum-well pulsed relaxation oscillator. Before joining Lincoln Laboratory in 1962, Chris was chief engineer at radio station WLLH-AM-FM in Lowell, Massachusetts. In 1965, he was instrumental in establishing the submillimeter laboratory under Peter Tannenwald, first using a hydrogen-cyanide gas discharge-laser, and later using a gas laser pumped with a carbon-dioxide laser. For thirty years, he was a mainstay of the Laboratory's submillimeter effort. He devised packaging designs and techniques for whisker-contacted micron-diameter quantum-well dots that facilitated the discovery of the resonant-tunneling-diode relaxation oscillator. Recently, this oscillator has been injection-locked to a sine wave and shown to be uniquely quiet in phase. Now enjoying semi-retirement (and a new granddaughter), Chris is engaged in a long-running home project to design and construct a standard-time reading sundial for an inside window sill. He studied engineering physics under Clarence Bennet at the University of Maine, Orono.